

Atomically thin optomemristive feedback neurons

Syed Ghazi Sarwat,^{1,2} Yingqiu Zhou,^{2,3} Jamie Warner,^{4,5} and Harish Bhaskaran²

¹⁾IBM Research – Europe, Säumerstrasse 4, 8803 Rüschlikon, Switzerland

²⁾University of Oxford, Parks Road, OX1 3PH, UK

³⁾Present Address: Denmark Technical University, Lyngby, 2800, Denmark

⁴⁾Texas Materials Institute, The University of Texas at Austin, 204 East Dean Keeton Street, Austin, Texas 78712, United States

⁵⁾Walker Department of Mechanical Engineering, The University of Texas at Austin, 204 East Dean Keeton Street, Austin, Texas 78712, United States

Cognitive functions such as learning in mammalian brains have been attributed to the presence of neuronal circuits with feedforward and feedback topologies. Such networks have interactions within and between neurons that provide excitatory and inhibitory modulation effects. In neuromorphic computing, neurons that combine and broadcast both excitatory and inhibitory signals using one nanoscale device is still an elusive goal. Here, we introduce a type-II heterojunction-based memristive neuron that demonstrates both these effects using optoelectronic charge-trapping mechanisms. We show that such neurons provide nonlinear and rectified integration of information, that can be optically broadcast. Such a neuron has applications in machine learning, particularly in winner-take-all networks. We then apply such networks on simulations to establish unsupervised competitive learning for data-partitioning, as well as cooperative learning in solving combinatorial optimization problems.

Keywords: Two-dimensional heterostructures, Optoelectronics, Chemical Vapour Deposition, Neuromorphic Computing, Winner-Take-All

INTRODUCTION

Neuromorphic computing hardware can both help us understand the brain by emulating it, and can increase efficiency of neural algorithms for artificial intelligence in data-centric applications^{1,2}. Simplified hardware emulations of threshold-based neuronal models are key to the realization of neuromorphic computing systems. However, emulating these with conventional CMOS, while possible is still inefficient. More recently scalable memristive devices, such as electronic and photonic phase change memory^{3,4}, Mott insulators^{5,6} and magnetic tunnel junctions⁷ have been explored. These can capture deterministic and stochastic neuronal dynamics towards compact and densely functional computing primitives. However, the physical attributes governing the dynamics in these devices are in contrast to the mechanisms governing biological neurons. In biological neurons, electrochemical mechanisms govern the membrane potential and this in turn regulates the communication and processing of information inside the cell⁸. Such an effect is capacitive in nature, implying that charges can be added and subtracted from the membrane, allowing both excitatory (depolarization) and inhibitory (hyperpolarization) effects. However, these are features complex to capture, for example, in phase change neurons, in which the membrane potential is driven by unidirectional crystal growth dynamics.

A single-device neuron that can more rigorously implement the neuronal dynamics can be realized if the mechanism governing its functionality correlates to the functioning of biological neurons. In this paper, we first demonstrate such a device using a type-II heterojunction based on two-dimensional (2D) materials. In such a device, the membrane potential is stored in the form of electronic charges on a capacitor. The capacitor, much like in biological neurons can store and integrate postsynaptic potentials on the millisecond timescale and can realize both excitatory and inhibitory functionality.

In particular, such excitatory and inhibitory signals can be used to perform computations⁹ that are challenging to implement using standard artificial neurons; these include neural gain mechanisms, neuronal voting, and winner-take-all learning (WTA). WTA, which is a category of computational models^{10–12} that invoke competitive stages during learning is of particular interest to modern machine learning^{13–15}. In a WTA computational unit, neurons can activate other neurons and propagate signals, as well as inhibit other neurons, making them less likely to fire messages of their own. This approach is powerful compared to standard approaches as a single computational unit adopting WTA dynamics can approximate multiple computational modules deploying standard sigmoidal type thresholding neurons. Current implementations of WTA networks with CMOS neurons only accommodate a single electrical signal, and thus require additional circuitry or software for implementing inhibition effects^{16–19}. A memristive neuron that provides built-in non-linearity, and accommodates in-memory excitatory and inhibitory effects, as well as broadcasting of inhibitory signals on neighboring (competing) neurons can allow efficient implementation of WTA learning. Crucially, we use these properties to simulate WTA networks for unsupervised competitive learning (CL^{13,20,21}) to solve a non-linear data partition, and in unsupervised cooperative learning to tackle the computationally difficult task of combinatorial optimization.

Optomemristive Neuron

We first show how a 2D heterostructure can be used to mimic a winner-take-all neuron, using both inhibitory and electrical excitatory signalling^{22,23}. For this, let us consider that the state of a biological neuron is represented by a membrane potential (u). This potential evolves as a function of the synaptic weighted inputs $I_{\text{feed-forward}}$ and $I_{\text{feed-back}}$. Specific to processes such as neuronal voting and winner-take-all learning, $I_{\text{feed-forward}}$ is a result of excitatory (Exc) feedforward connections that allows one to maintain and amplify input patterns, while $I_{\text{feed-back}}$ emerges from inhibitory (Inh) signals, which in combination with the excitory signals form a neuronal motif. When both these effects are considered, the dynamics of the neuronal state in an integrate and fire neuron model follow $\frac{du}{dt} \propto f(W \times I_{\text{feed-forward}} + M \times I_{\text{feed-back}})$. Here, W and M are the input resistance (weight) matrices for feed-forward and feedback connections respectively. Using this, $u(t)$ captures a range of neuronal processes. In this optomemristive neuron, we implement these features of excitory–inhibitory and inhibitory data signalling on our 2D heterostructure. Effectively, whilst the excitory signals are maintained using the charge (u_n) within the nanoscale device, the evolution (time-dependent gradient) of the charge is governed by the optoelectronic properties of the type-II heterojunction. We use global free-space optical signalling to achieve inhibition in this work²⁴.

Our type-II heterojunction is a vertical heterostructure comprising two-dimensional WS₂ and MoS₂ materials. In analogy to biological neurons (see Figure 1a), the heterojunction serves as the neuronal membrane and the graphene electrodes as the soma; the state is represented in the soma, but modified by the changes in the membrane. In effect, such a concept can be abstracted as a single-device voltage dependent current source (see Figure 1b-c, in which the channel conductance (g_c) changes with u_n . u_n can be altered, that is increased and decreased by applying short electrical and optical pulses based on the excitory and inhibitory inputs, respectively. In Figure 2a we illustrate these mechanisms. The band-offsets between WS₂ and MoS₂ create an intrinsic field. When an optical signal (O_L) is applied (see left panel of Figure 2a), charge carriers are generated and consequently separated by this field. The absence of carrier recombination in such a configuration leads to an increase in the electron charge concentration ($u_{n(e)}$) in the channel, via two mechanisms: photogating and photoconductive effects^{25–28}. In response, the Fermi energy (E_F) in the channel is altered^{29,30} (increased). A positive electrical gate voltage (V_G) allows for a reverse process (see right panel of Figure 2a). Under the action of external field, the holes recombine with the excess carriers in the channel to decrease $u_{n(e)}$, and retrieve E_F . This is illustrated further on a calculated potential energy landscape in Figure 2b. The figure shows two hole-trap states above the valence band of MoS₂. The (de)trapping of holes provide a shift in the channel's E_F (see Methods Section).

Crucially, when V_G is the excitory input and O_L is the inhibitory input, $\frac{du_{n(e)}}{dt}$ maps the change in the channel conductance to the type of inputs and/or their combinations. The neuron accepts electrical ($+V_G$) and optical spikes (O_L) as inputs. Each input produces a discrete transition in the state variable u . Combining with an analytical model (see Supplementary Figures S1-S2), such state transitions are described in Figure 2c. Here, the channel resistance increases and decreases with O_L , and V_G inputs respectively. The state-change delay is governed by the RC time constants for change in $u_{n(e)}$.

In the following sections, we present experimental verification of such a concept. The fabrication process for the devices is illustrated schematically in supplementary section S2. All 2D materials are monolayered which we verify using Raman and photoluminescence (PL) measurements. When the vertical pads are contacted as sourcing and drain terminals, the current across the G_T channel is read out (see the inset in Figure 2d; the different materials are color coded). In Figure 2e, PL spectra corresponding to these regions are plotted (also see supplementary Figures S3-S5). Strong photoluminescence quenching^{31,32} is noted when the TMDs are combined. These results indicate decreased recombination probabilities of the photoexcited charge carriers in the TMDs, indicative of type-II band-offsets that perform charge separation, in addition to electron transfer into graphene. Besides being the most photoabsorbing stack owing to the presence of two semiconductors, the heterostructure WS₂-MoS₂-G_T expresses both of these effects. In the remainder of the manuscript we focus on this stack type.

Device Characterization

The device measurement scheme is illustrated in Figure 3a for a WS₂-MoS₂-G_T device. The channel state is measured using source-drain (V_{SD}) read signals on G_T. The channel is electrostatically coupled to the substrate, with G_T acting as one plate of a capacitor and the Si substrate, the other. The channel conductance is altered using V_G signals. Figure 3b plots the transfer characteristics of a device before and after illumination. The G_T channel exhibits an ambipolar-type carrier transport and is p-doped as the minimum conductance or the charge neutrality point (V_{CNP}) is positive. By optically illuminating the device, the V_{CNP} shifts to smaller turn-on voltages (dotted trace). At zero gate -which is the read-out signal- this then corresponds to a decreased I_{SD} . Crucially, this is an increase in channel resistance, and thus is an inhibitory effect. We observe the change in the charge neutrality point (ΔV_{CNP}) to increase with the irradiance (see Figure 3c). Both these effects indicate a change in

the carrier concentration, i.e. $\Delta V_{\text{CNP}} = \frac{\Delta u q}{C}$, where q is the elementary charge and C is the capacitance, and is constant in the device. The change in ΔV_{CNP} is notably significant ($\approx 85\%$ relative change) under modest optical power ($5 \mu\text{W}$ at 532 nm).

When viewed in a 2 terminal configuration, it becomes clear that the device functions as a memristor (see supplementary information Figure S6). However, its behaviour is of a type that exploits both externally applied electric field and light for switching between low (LRS) and high (HRS) resistance states (see Figure 3d). In LRS, a $-V_G$ spike increases I_{SD} , while a $+V_G$ spike decreases it (see Figure 3e). This response is transient (volatile) and lasts as long as the pulse. In HRS, however, the device responds differently. Figure 3f plots the I_{SD} for increasing *sign* V_G . While for $-V_G$, the change in I_{SD} remains volatile, for $+V_G$ spikes, the change is non-volatile, i.e. I_{SD} increases, taking a new temporally stable value. Additionally, and as in analog neurons, the device exhibits an accumulative property (see Figure 3g). When subjected to a train of identical (both in amplitude and width) $+V_G$ spikes, the device progressively transitions from HRS to LRS. A reverse effect that is an accumulated transition from LRS to HRS is also achievable, however and distinctly, through optical excitation. Starting in the LRS state, the resistance of the device increases when subjected to identical optical spikes ($5 \mu\text{W}$ at 532 nm) in the absence of a V_G signal. The process repeats until a stable state (the HRS) is achieved. In the HRS state further optical exposure results only in a volatile increase of resistance, that lasts as long as the pulse (see Figure 4a). While there is effectively no limit to generating photoexcited carriers, there is an upper bound to how many of the carriers can be effectively trapped. This threshold is determined by the available hole-traps. Using $\max(\Delta V_{\text{CNP}})$ we estimate this to be of the order of $1.2 \times 10^{16} \text{ m}^{-2}$.

In Figure 4b we elaborate the mechanism that results in the excitory and inhibitory transitions. When optical pulses are sent (see top panel of Figure 4b), photoabsorption in the MoS_2 and WS_2 layers results in carrier generation, contributing to $\Delta u_n = u_{\text{nex}(e)} + u_{\text{nex}(p)}$, where $u_{\text{nex}(e/p)}$ represents the excess electrons and holes in the TMDs respectively. The field and potential landscape within the device provides charge separation, such that $u_{n(e)}$ number of electrons inject into graphene, while $u_{n(p)}$ number of holes move to the substrate interface, where they are effectively trapped. These localized holes cannot be recombined thereafter and hence via the photogating effect induce electrons in graphene. Thus, even after the optical pulse is turned off, a residual charge exists in the channel, which lowers p-doping in G_T , and thus conductance of the channel, resulting in the inhibitory operation (see bottom panel of Figure 4b). Here, the residual charge concentration $\Delta u_{n(\text{res})} \propto \eta P t$ scales with the incident optical flux (P), exposure time (t) and photoelectric conversion efficiency (η), where $\Delta u_{n(\text{res})} < \Delta u_n$. The conversion efficiency is a function of the absorption coefficient and charge separation. When a positive V_G pulse is applied, the electron (hole) concentration in the channel (substrate interface) increases due to a back-gate field effect. The accumulated carriers follow $\Delta u_{\text{res}(e/p)} = \frac{\epsilon \epsilon_r V_G A}{t_{\text{ox}}}$, where ϵ and ϵ_r are vacuum and relative permittivities for substrate SiO_2 respectively, t_{ox} its thickness and A is the device area. In addition, recombination between the field-generated electrons and the previously localized holes occur when the gate is turned on such that $\Delta u_{n(\text{res})}$ decreases. Thus, when switching off the optical pulse, the channel current increases due to the diminishing of the photogating effect, resulting to an excitory operation.

Compared to the inhibitory operation which was governed by the properties of the TMDs and the junction, the excitory operation is dictated by the geometry of the devices and properties of the substrate. The mechanisms discussed in Figure 4b can be correlated to experimental data in Figure 4c. The figure illustrates a device's response to both electrical and optical signals. Starting in HRS, a $+V_G$ input switches the device to an intermediate HRS. This state is non-volatile and temporally stable. Subsequently, when subjected to an optical pulse the device reverts to HRS. The transient features can be adequately fitted to a double exponential function with comparable time constants (τ_1 and τ_2). Overall, we have good control in our ability to program the device to different resistance states. For example, starting in HRS, different states can be programmed simply by changing the amplitude of V_G pulses (see Figure 4d), and be RESET fully or partially using suitable optical pulses (also see supplementary information Figure S7). Moreover, the devices allow programmability using both pulse width and amplitude modulation methods, which are standard input spike encoding schemes in neuromorphic systems. Figure 4e shows pulse width modulation viz $30 V_G$ excitory spike of widths (100 ms to 1000 ms) switch the device to conductive states.

Competitive Learning

Machine learning has traditionally focused on learning algorithms which require labelled data or rewards. Autonomous intelligence, however, works without them, and therefore make continuous learning possible. Using simulations we now discuss how the heterojunction device conceptually enables neuromorphic computing frameworks for autonomous intelligence. As a first example, the implementation of unsupervised CL learning^{16,33} is described. CL learning requires WTA computational models by which neurons compete with each other for activation (excitation). The system consists of a neural network, as represented in Figure 5a. The network propagates the input to the competing layer, comprising WTA neurons- the output of each neuron indicates which cluster an input data pattern belongs to. Each neuron performs the task of accumulation and activation, of the form $N_j = \sum_{i=1}^n f(b + X_i W_{ij})$, where X_i represents the input pattern, b is a bias term and W_{ij} is the weight of excitory synapses to the N_j neuron. Learning occurs only when the network selects the neuron(s) with the highest activation, and synaptic weights

of only those with the highest activation are updated. This can occur in an unsupervised manner when the neurons mutually inhibit each other, such that an update rule of the form of $\Delta W_{ij} = \alpha \times (X_i - W_{ij}) \times \xi$ becomes applicable. Here α is the learning constant, and $\xi = \begin{cases} 1, & \text{if } N_j > N_k; j \neq k \\ 0, & \text{otherwise} \end{cases}$ encodes the global inhibition effects, i.e. the winner neuron activates itself while simultaneously inhibiting others.

For purposes of providing clarity, we illustrate these WTA dynamics using two interacting (N_1 and N_2) neurons (see the top panel in Figure 5b and Methods Section). We now discuss the emulation of these features using the devices as WTA neurons (see the bottom panel in Figure 5b). The excitory input to the devices are the V_G pulses, and a device is said to fire if the change in its channel current (ΔI_{SD}) exceeds some threshold. The inhibitory connections between the devices are free-space optical signals. Similar to before, without inhibition both devices fire together, however, when inhibition is included, the channel of N_2 is inhibited (ΔI_{SD} becomes marginal). Thus, the device offers two intrinsic device properties that contribute to the neuronal activation. First is the excitory electronic switching from V_G (where V_G encodes the weighted sum of inputs), and second is the device's inherent non-linearity in its ΔI_{SD} - V_G characteristics, which remarkably realizes a memristive implementation of a rectified activation function (see Methods Section). This is illustrated in Figure 5c (the dotted traces represent a fit to the data).

A sketch of a conceptual hardware framework exploiting these features is sketched in Figure 5d (also see Methods Section). Figure 5e illustrates the task that we solve, which is to unmix input data patterns by clustering them into three different classes. The example here is that of categorizing three classes (eg. flower type) based on their dominating distinct features (eg. sepal length, width, weight). Each input is a vector of three elements and is custom generated. In the figure, the inputs are color-coded, and they are clustered together depending on their similarities. Before training the output neurons, represented by the norm vector of $||W_{ij}||$, where i and j are indexes for neurons in the input and output layer, respectively, are randomly placed, and no neuron tends to any specific input data pattern. Through iterative learning, the neurons learn the data set features, and they change their synaptic configuration in tune with the input. The effect of WTA is made more evident in the final layer of the network (not shown) that performs a softmax activation on the outputs of the competitive layer (see Figure 5e). Without CL, independent of the input, all neurons activate with similar probabilities (mean of 50 measurements in each case is shown), thus lacking the ability to cluster input data. With CL, the inhibitory effects allow the network to learn without backpropagation, and the probability of neurons firing is selectively increased for specific input patterns.

Cooperative Learning

We now demonstrate the scheme of cooperative learning (CoL), which is yet another WTA mechanism (see Figure 5f-h), to further highlight the potential of global optical signaling. In contrast to CL, in CoL not only the weight vector of the winner neuron is updated, but also the weights of select neighbouring neurons³⁴. Weight updates follow the expression $W \leftarrow W_i + \alpha(t)h_{(i,c)(t)}(x - W_i)$. Here $h_{(i,c)}$ describes a neighbourhood function. This is, therefore, a form of a soft WTA mechanism, however, one that specifically requires a reconfigurable softness defined by a time-dependent learning rate ($\alpha(t)$). The neighbourhood function is a critical factor in the algorithm; it defines the nature and extent of lateral connections. Accordingly, a new learning constant can be defined, representing $\alpha' = \alpha_o(t) \times h_{ic}(t)$, where $c(x)$ is the winner neuron and i represents all other output neurons. For learning to occur, the neighbourhood factor must be a decreasing function as a function of iteration.

For example, the function $h_{ic}(x) = \begin{cases} 1, & \text{when } i_n \subseteq N_c \\ 0, & \text{when } i_n \not\subseteq N_c \end{cases}$, defines a box kernel around the winner neuron c , where N_c is the index set of the neighbor nodes around the winner neuron defined by a radial distance r_c . Only the neurons within r_c are updated during the learning phases. Importantly, during learning r_c must decrease with each iteration, and all the select neurons must be tracked for updates. This incurs significant computational overheads. Our scheme of using free-space optical signalling for neighborhood function provides a solution.

The intensity of optical signals follow $P(r) \propto P_o \exp(-\Omega v r^3)$, where Ω is a solid angle subtended by the light beam and v is the attenuation coefficient in the propagation medium. Crucially, this expression represents a radial function of radiance from inverse square decay and attenuation mechanisms. This suggests that the amplitude of the optical signals can be spatially constrained. For CoL, $P(r,t)$ in the format of a reconfigurable neighborhood function can be achieved simply by amplitude modulation (changing $P_o(t)$), and using binary thresholds in the optoelectronic neuronal units to sense light (see supplementary Figure S8). Following the same ideas used in CL, in the implementation of CoL, the winner neuron broadcasts an optical pulse (O_L). However, the signal is excitory and spatially constrained, i.e. neurons which receive a threshold amount of light are only updated. Notably, this approach, therefore, achieves the feature of both reconfigurable softness and in-memory updates.

To demonstrate the usefulness of such an approach, we perform the computationally difficult traveling salesman problem.

This is a problem of combinatorial optimization, which is NP (non-polynomial) hard. The task is of finding the shortest route possible that traverses all cities on a given map, however, only once. To solve it, we embed the problem into a self-organizing map³⁵ (also see supplementary information section S8). Initially, all WTA neurons are randomly assigned. After learning, the synaptic weights of the neurons evolve such that every unique neuron learns the coordinates of a unique city, i.e. a neuron and a city become assigned to each other. This means the synaptic weights take the values of the geographic coordinates. As the solution to the problem evolves, the output neurons cooperate with each other for updates using the lateral connections. In the beginning several neurons learn, and as iterations proceed learning occurs more and more locally since the neighborhood gets smaller and smaller from decreasing $P_O(t)$. Using these concepts, the algorithm arrives at an optimized route (see Figure 5i).

CONCLUSION

Neuronal emulation requires the non-linear integration of excitatory and inhibitory postsynaptic potentials. This combination of non-linearity and integration has not been previously shown for in-memory computations; whilst conventional charge-based photodetectors can operate in the mixed-mode, i.e. their photosensitivity can be modulated by electrical signals and vice versa, they lack the two key properties required to integrate data-stream for computations. The optomemristive neuron provides a rectified type non-linearity in its output characteristics, i.e. the output scales with the input only for positive inputs. This is a type of non-linearity commonly required in all modern neural networks. While recently, thermal heater based memristors have been suggested for activation neurons, they achieve the required activation only through added energy-inefficient direct current offsets³⁶. Some important challenges, however, should be considered when considering scaling up such an approach. To meet the requirements for on-chip integration, individual WTA neurons need to be of micrometer size, as well as allow reconfigurable receptive fields for implementing global and local learning. One approach to realizing such neurons is via monolithic integration of the electronic units with micro-light emitting diodes^{37,38} (also see supplementary Figure S9-S15). There is also the challenge of accommodating the one-to-many inhibitory signalling. Compared to CL, CoL requires finer optimization of the hyperparameters, including the type of the neighbourhood function. While the operational parameters described in this work require further research into how they can be implemented at a system level, this work provides a framework for a future design using both optical and electrical stimuli within engineered heterostructures. In summary, we have described a framework of atomically thin heterojunctions as optomemristive neurons, which can implement inhibitory and excitatory neuronal processes.

ACKNOWLEDGEMENT

We acknowledge funding for this work from the European Union's Horizon 2020 Research and Innovation Programme (HyBrain project no. 101046878), EPSRC through grants EP/R001677/1, EP/M015173/1, and EP/J018694/1, and from the European Research Council through the grant no. 725258.

AUTHOR CONTRIBUTION

S.G.S. and Y.Q. carried out the experiments and analysis. Y.Q. fabricated the devices. S.G.S. conceptualized and performed device and ML simulations. S.G.S., Y.Q., J.H.W., and H.B. discussed the data and wrote the manuscript. J.H.W. and H.B. supervised the research.

COMPETING INTERESTS

The authors declare no competing interests. H.B. is a founder and holds shares in Saliency Labs Ltd.

METHODS

Device fabrication and measurements: The devices use monolayered chemical vapour deposition method grown WS_2 , MoS_2 and graphene on 300 nm SiO_2/Si substrate. Our fabrication procedure is such that it allows us to create vertical heterostructures with different combinations of materials; this per device - two are vertically oriented and two are horizontally oriented. The recipes describing the material synthesis, and the fabrication process flow are presented in the supporting information (Supplementary Figure S3). The optoelectronic measurements were performed using a custom-built probe station that comprised a confocal microscope for device illumination. A 532 nm diode-pumped solid-state laser (Thorlabs, DJ53240) was coupled into the microscope to form a beam with a spot size of $\approx 150 \mu\text{m}^2$. For the electrical read out we used Keithley 2400 and

Keithley 2614 B sourcemeter units. The Si substrate was used as the back-gate and the source graphene was grounded in all our measurements. Custom python and LabView programs were used for the experiments. The device(s) exhibit ‘memory’ properties in LRS for optical stimulation, in HRS it exhibits a photoconductive mode of operation. Noting that the residual charges in the device are created by photoexcitation and trapping, this effect arises from the decline in the photogating mechanism, which we modelled in Figure 2 using the equation $\Delta E_F = h\nu_F \sqrt{\Delta u_{n(e)}\pi}$, where h and ν_F are Planck’s constant and Fermi velocity, respectively. In other words, the more pronounced the photoabsorption and trapping effects in the device, higher is the shift in V_{CNP} (E_F). This occurs through state value increases. An electrical spike increments ($+\delta u$) the state variable through accumulation (Σ), while with the optical input decreases ($-\delta u$) the state variable through accumulation.

Feedback driven learning: In Figure 5, we model the neurons to be phase-locked leaky-integrate and fire type. The interactions between the neurons are such that N_1 can inhibit N_2 , at time instances where it fires ($\delta(t - t_0)$), i.e. N_1 is the winner neuron in the network. Thus, without inhibition N_1 and N_2 fire together, but when an inhibition knob is turned-on the action potentials in N_1 hyperpolarizes N_2 , such that it is inhibited from firing. Note that in our simulation of the network using device-level data we refer to inhibition as a process that cancels or attenuates an excitory input (state) of the neuron. This simplest WTA computational module is a hard winner-take-all network, where only a single neuron in the network becomes active at the expense of neighbouring neurons, which it inhibits. Thus, in a network of neurons, the neuron with the highest activation can optically inhibit all other neurons, such that their output decrease and none of the synaptic weights corresponding to the “losing” neuron are updated. In Figure 5c we illustrate electrically stimulated activation of a heterojunction-II device (the trace colored in brown). For implementing global inhibition, we utilize the inhibitive photobehavior (the trace colored in black). This is

modelled using, for $\Delta I_{SD} = \begin{cases} f(x), & \text{for } +V_G \\ 0, & \text{for } 0 \text{ and } -V_G \end{cases}$, where $f(x) = V_{Gate}^\beta$, $\beta \leq 1$ for analog encoding, and $f(x) = n_i^p + n_i^q$, with

$p, q \leq 1$ for spike train (number of spikes n) encoding. For the classification task the inputs are vectors $\mathbf{v}=[v_1, v_2, v_3]$ where, $v_n : 0-1$, and which are represented in the format of normalized Euclidean space ($||v||$). In our implementation of cooperative learning, the devices encode the weight matrix, and the sense unit which operates on and accumulates the feedforward signal. Each neuronal unit further comprises a standard CMOS photosensitive unit for light detection and generation which represent the feedback signals. Crucially, the synapses either strengthen or disappear during learning, under the control of the received inputs. The SOM is comprised by a layer of standard input neurons and a layer of WTA output neurons, which are mapped into a single crossbar array. To this array, the feedforward signals are electrical signals which perform matrix vector multiplication for synaptic weighing, while the lateral feedback signals between the output neurons is realized using optics. This feedback implements the box neighbourhood function. The number of WTA neurons equal to the number of cities for which the problem is solved for, and the latitudes and longitudes of 20 major cities in Switzerland comprise the input vectors to the network.

DATA AVAILABILITY

The data that support the findings of this study are available from the corresponding author upon reasonable request.

REFERENCES

- ¹Merolla, P. A. *et al.* A million spiking-neuron integrated circuit with a scalable communication network and interface. *Science* **345**, 668–673 (2014).
- ²M, D., N, S., T, L. & G, C. Loihi- a neuromorphic manycore processor with on-chip learning. *IEEE Micro* **38**, 82–99 (2018).
- ³Tuma, T., Pantazi, A., Le Gallo, M., Sebastian, A. & Eleftheriou, E. Stochastic phase-change neurons. *Nature Nanotechnology* **11**, 693 (2016). URL .
- ⁴Feldmann, J., Youngblood, N., Wright, C. D., Bhaskaran, H. & Pernice, W. H. All-optical spiking neurosynaptic networks with self-learning capabilities. *Nature* **569**, 208–214 (2019).
- ⁵Kumar, S., Williams, R. S. & Wang, Z. Third-order nanocircuit elements for neuromorphic engineering. *Nature* **585**, 518–523 (2020).
- ⁶Yi, W. *et al.* Biological plausibility and stochasticity in scalable VO_2 active memristor neurons. *Nature communications* **9**, 1–10 (2018).
- ⁷Hassan, N. *et al.* Magnetic domain wall neuron with lateral inhibition. *Journal of Applied Physics* **124**, 152127 (2018).
- ⁸Kandel, E. R. *et al.* *Principles of neural science*, vol. 4 (McGraw-hill New York, 2000).
- ⁹Yin, H. The self-organizing maps: background, theories, extensions and applications. In *Computational intelligence: A compendium*, 715–762 (Springer, 2008).
- ¹⁰Maass, W. On the computational power of winner-take-all. *Neural computation* **12**, 2519–2535 (2000).
- ¹¹Maass, W. Neural computation with winner-take-all as the only nonlinear operation. *Advances in neural information processing systems* **12**, 293–299 (2000).
- ¹²Lazzaro, J., Ryckebusch, S., Mahowald, M. A. & Mead, C. A. Winner-take-all networks of $O(n)$ complexity (1988).
- ¹³Kaski, S. & Kohonen, T. Winner-take-all networks for physiological models of competitive learning. *Neural Networks* **7**, 973–984 (1994).
- ¹⁴Gerstner, W., Lehmann, M., Liakoni, V., Corneil, D. & Brea, J. Eligibility traces and plasticity on behavioral time scales: experimental support of neohebbian three-factor learning rules. *Frontiers in neural circuits* **12**, 53 (2018).
- ¹⁵Ferguson, K. A. & Cardin, J. A. Mechanisms underlying gain modulation in the cortex. *Nature Reviews Neuroscience* **21**, 80–92 (2020).
- ¹⁶Kreiser, R., Moraitis, T., Sandamirskaya, Y. & Indiveri, G. On-chip unsupervised learning in winner-take-all networks of spiking neurons. In *BioCAS*, 1–4 (2017).

- ¹⁷Hsu, D., Figueroa, M. & Diorio, C. Competitive learning with floating-gate circuits. *IEEE Transactions on Neural Networks* **13**, 732–744 (2002).
- ¹⁸Diehl, P. U. & Cook, M. Unsupervised learning of digit recognition using spike-timing-dependent plasticity. *Frontiers in computational neuroscience* **9**, 99 (2015).
- ¹⁹Ebong, I. E. & Mazumder, P. CMOS and memristor-based neural network design for position detection. *Proceedings of the IEEE* **100**, 2050–2060 (2011).
- ²⁰Srivastava, R. K., Masci, J., Kazerounian, S., Gomez, F. J. & Schmidhuber, J. Compete to compute. In *NIPS*, 2310–2318 (Citeseer, 2013).
- ²¹Oster, M., Douglas, R. & Liu, S.-C. Computation with spikes in a winner-take-all network. *Neural computation* **21**, 2437–2465 (2009).
- ²²Fenno, L., Yizhar, O. & Deisseroth, K. The development and application of optogenetics. *Annual review of neuroscience* **34**, 389–412 (2011).
- ²³Gradinaru, V. *et al.* Molecular and cellular approaches for diversifying and extending optogenetics. *Cell* **141**, 154–165 (2010).
- ²⁴Sarwat, S. G., Moraitis, T., Wright, C. D. & Bhaskaran, H. Chalcogenide optomemristors for multi-factor neuromorphic computation. *Nature communications* **13**, 1–9 (2022).
- ²⁵Wang, Q. *et al.* Nonvolatile infrared memory in MoS_2/PbS van der waals heterostructures. *Science advances* **4**, eaap7916 (2018).
- ²⁶Xiang, D. *et al.* Two-dimensional multibit optoelectronic memory with broadband spectrum distinction. *Nature communications* **9**, 1–8 (2018).
- ²⁷Tran, M. D. *et al.* Two-terminal multibit optical memory via van der waals heterostructure. *Advanced Materials* **31**, 1807075 (2019).
- ²⁸Lee, J. *et al.* Monolayer optical memory cells based on artificial trap-mediated charge storage and release. *Nature Communications* **8**, 1–8 (2017).
- ²⁹Sze, S. M., Li, Y. & Ng, K. K. *Physics of semiconductor devices* (John Wiley & sons, 2021).
- ³⁰Amit, I. *et al.* Role of charge traps in the performance of atomically thin transistors. *Advanced Materials* **29**, 1605598 (2017).
- ³¹Kim, S. Y., Yang, H. I. & Choi, W. Photoluminescence quenching in monolayer transition metal dichalcogenides by Al_2O_3 encapsulation. *Applied Physics Letters* **113**, 133104 (2018).
- ³²Li, Z., Wang, W., Greenham, N. C. & McNeill, C. R. Influence of nanoparticle shape on charge transport and recombination in polymer/nanocrystal solar cells. *Physical Chemistry Chemical Physics* **16**, 25684–25693 (2014).
- ³³Carpenter, G. A. & Grossberg, S. A massively parallel architecture for a self-organizing neural pattern recognition machine. *Computer vision, graphics, and image processing* **37**, 54–115 (1987).
- ³⁴Kohonen, T. Essentials of the self-organizing map. *Neural networks* **37**, 52–65 (2013).
- ³⁵Kohonen, T. The self-organizing map. *Proceedings of the IEEE* **78**, 1464–1480 (1990).
- ³⁶Oh, S. *et al.* Energy-efficient mott activation neuron for full-hardware implementation of neural networks. *Nature nanotechnology* **16**, 680–687 (2021).
- ³⁷Meng, W. *et al.* Three-dimensional monolithic micro-led display driven by atomically thin transistor matrix. *Nature Nanotechnology* **16**, 1231–1236 (2021).
- ³⁸Hwangbo, S., Hu, L., Hoang, A. T., Choi, J. Y. & Ahn, J.-H. Wafer-scale monolithic integration of full-colour micro-led display using mos_2 transistor. *Nature Nanotechnology* **17**, 500–506 (2022).

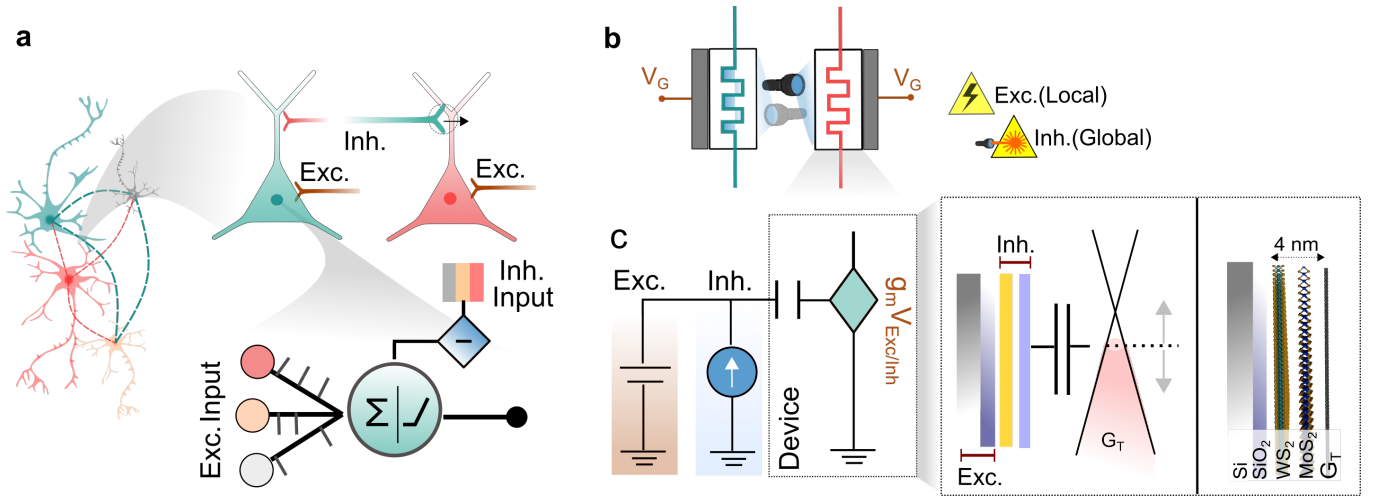


FIG. 1: Competitive Neuron Concept. (a) Schematic of biological neuron model that consists of excitatory and inhibitory inputs. The inhibitory connections are established via one-to-all signalling. Bottom panel: A neuron performs summation and non-linear operation on the excitatory inputs. In contrast, the inhibitory inputs provide a subtractive effect. (b) Illustration of an artificial type-II heterojunction neuron. The excitory signals are electrical and local to individual neurons, while the inhibitory inputs are optical and can be global. (c) Left panel: the artificial neuron can be approximated as a voltage-dependent current source, in which the charge on a capacitor modulates the channel's conductance. Excitory and inhibitory inputs change the charge concentration on the capacitor. Middle panel: In a vertical heterojunction device, the excitory inputs are electrical gate voltages, and the inhibitory signals are optical pulses. Distinct components in the device respond to either signal. The conductance of the graphene (G_T) channel is electrostatically modulated via the inherent device capacitance. Right panel: A sketch illustrating the different materials comprising a vertical heterojunction device.

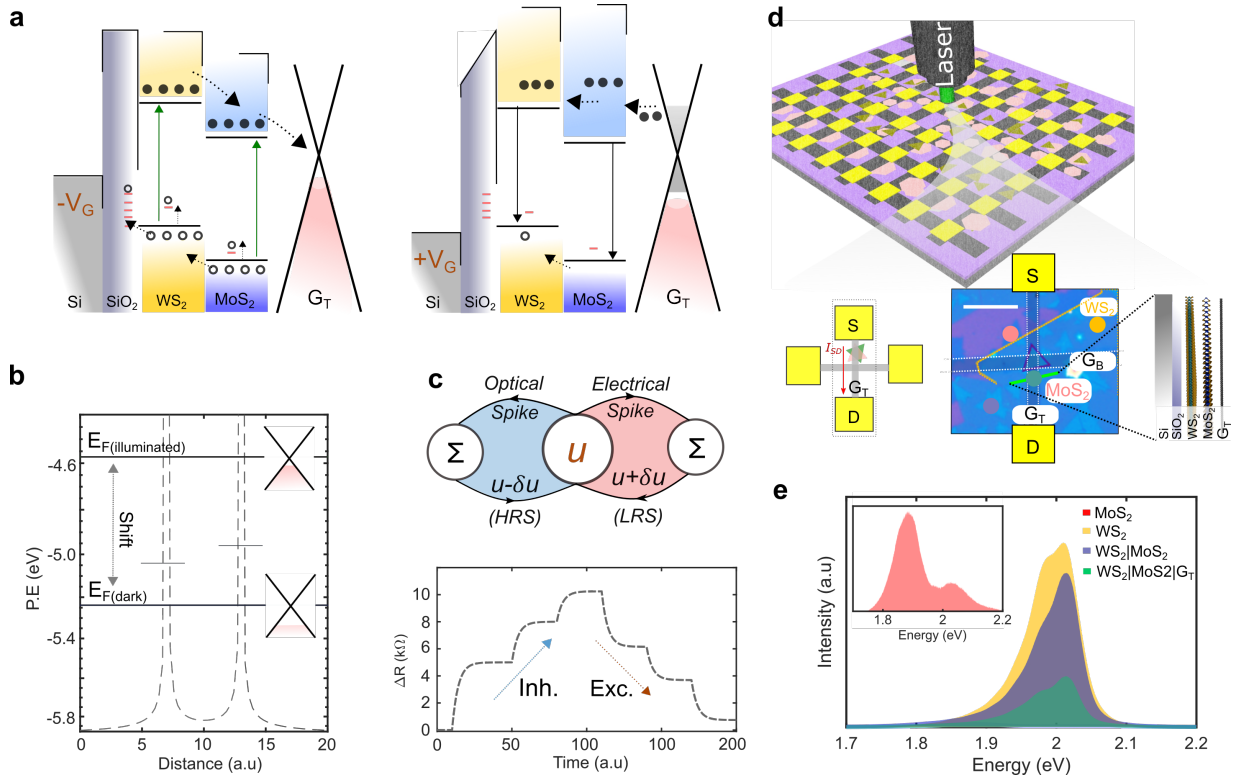


FIG. 2: Type-II heterojunction neuron . (a) Left panel: Energy band diagram illustrating the inhibition effect in the device. Optically excited electrons in WS_2 and MoS_2 transit into G_T and holes to the substrate, both resulting in increased charge concentration in G_T . Right panel: Energy band diagrams illustrating the excitory effect. Previously trapped holes and electrons recombine under a positive gate signal leading to a decreased charge concentration in G_T . (b) A simulated potential landscape showing Fermi level shift in the G_T channel depending on the filling of the holes traps (black filled region). (c) Top panel: The top panel is a state diagram of a competitive neuron. The inputs are electrical and optical spikes. Each input type produces a discrete transition (excitatory or inhibitory) in the state variable u . With an electrical spike, the state variable is incremented (the device approaches LRS), while for an optical input, the state variable is decremented (the device approaches HRS). The bottom panel illustrates a simulated dynamic response of the vertical heterojunction neuron to inhibitory and excitory inputs. (d) A schematic illustrating the optoelectronic measurement. Inset shows the measurement configuration and sketch of a WS_2 - MoS_2 - G_T heterostructure device that is electrically read-out using the vertical source and drain pads. An optical micrograph of such a device is also shown. The different materials are annotated. (e) Photoluminescence spectra of TMDs and their stacks. The quenching in the photoluminescence indicates inter-layer charge separation.

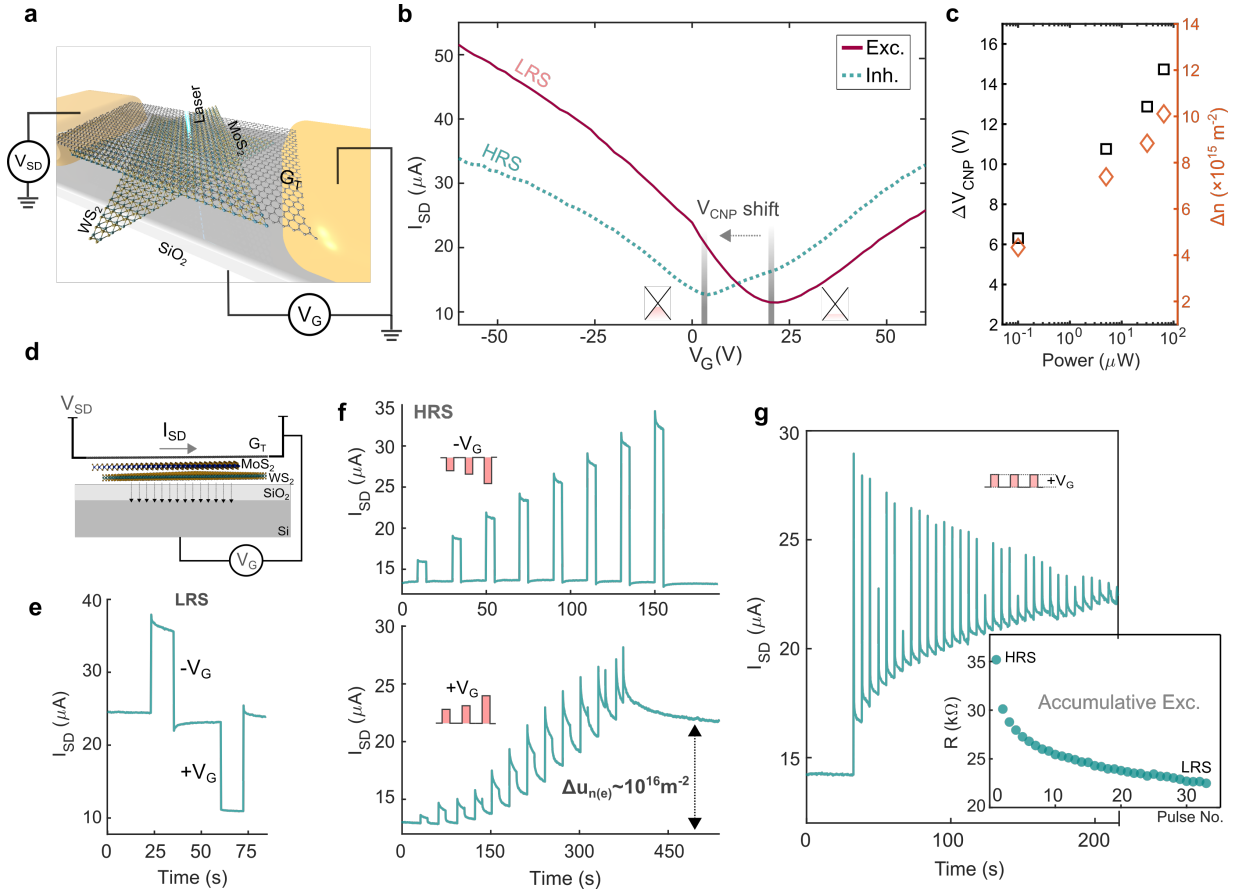


FIG. 3: **Excitatory Characteristics.** An illustration of the optoelectronic measurement. (b) Transfer characteristics curves of a type-II heterojunction-based device after excitory input and inhibitory inputs. (c) A scatter plot showing the shift in CNP in the heterojunction device under increasing irradiance. The arrow indicates increase in the charge concentration of trapped carriers. (d) An illustration of the electronic measurement for excitory input. (e) Transient response of the LRS state of the heterostructure to +30 and -30 V_G pulses. (f) A transient response of the HRS state of the heterostructure to - V_G (top panel) and + V_G (bottom panel). (g) A plot illustrating the electrical accumulative property of the device. Inset shows the progressive decrease in the channel resistance from repeated electrical excitory pulses.

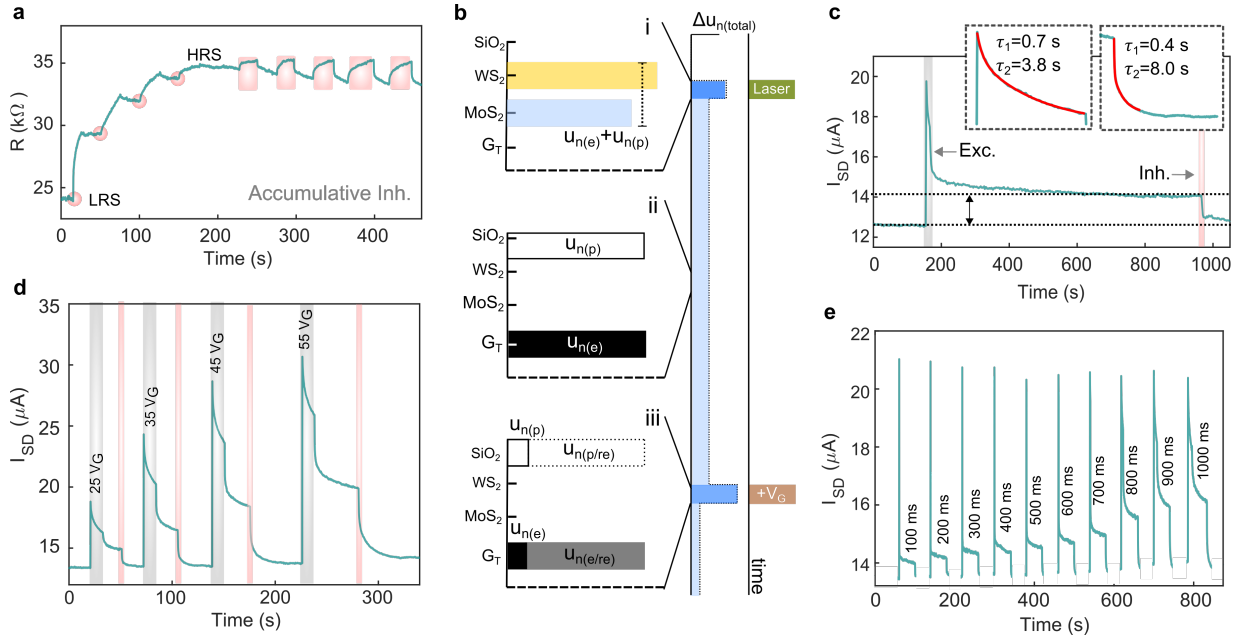


FIG. 4: Excitatory and Inhibitory Characteristics. A plot illustrating the optical accumulative property of the device in the absence of a gate signal, i.e. an increase in channel resistance from repeated inhibitory signals. (b) A schematic illustration of the time evolution of the carriers' concentration and their spatial distribution in the device. When an optical signal (laser) pulse, acting as the inhibitory signal, is applied, the carrier concentration in the device increases (shown in the top panel). This is a result of photoexcitation in the heterojunction; that is in the MoS₂ and WS₂ layers. After the optical signal is removed, an increased carrier concentration is maintained because of the charge trapping effects. Specifically, from the accumulation of holes at the interface of SiO₂ and WS₂ (shown in the middle panel). Here, the holes are represented by a white box and electrons with a black shaded box. After an electrical gate pulse, acting as the excitory signal is applied to the device, the carrier concentration then decreases. More specifically, this is due to the recombination between the trapped holes and electrons in graphene. The decrease is highlighted by the dotted and gray boxes, for holes and electrons, respectively. (c) A graph showing the optoelectronic mode of device operation using a gate and optical pulse. Insets are fit to the decay tails of the resistance transitions. The double sided arrow indicates change in the channel's conductance. (d) A plot illustrating reversible switching between multiple non-volatile resistance states using repeated excitory and inhibitory pulses. The pulse amplitude of excitory signals is varied. (e) A plot illustrating reversible switching in the device under varying width of the excitory pulses.

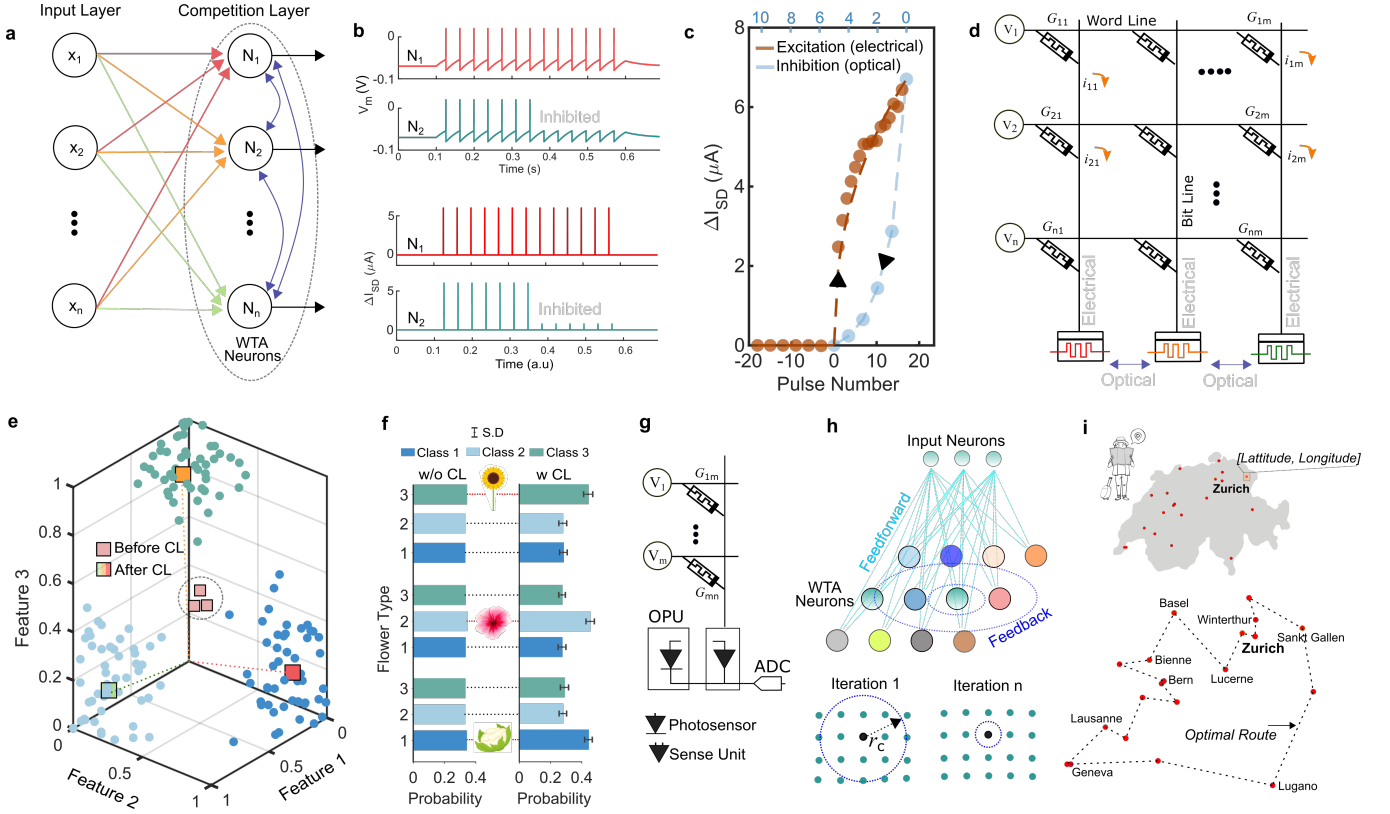


FIG. 5: Winner-take-all learning. An illustration of a two-layer competitive neural network. The output layer comprises WTA neurons. (b) The top panel shows biological excitatory and inhibitory connections between two neurons (N_1 and N_2), and simulated neuronal firing with and without inhibition. The bottom panel shows a synthetic implementation of these properties using optomemristive neurons. (c) A plot highlighting neural non-linear activation (excitatory response) behavior of a heterojunction device as a function of V_G polarity and pulse number, and the reverse inhibition effect. (d) A memristive crossbar comprising optomemristive neurons and synapses. Electrical excitation occurs at the columns and optical inhibition occurs between the output neurons in free space. (e) An illustration of a conceptual CL process for the task of clustering input data patterns (colored circles in the Euclidean space) into three classes. The synaptic weight vector to each WTA output neuron is represented as a colored square before and after learning using excitatory and inhibitory effects. (f) Bar charts illustrating the firing strengths (probabilities) of three output neurons in the task of clustering flowers depending on their dominant and distinct feature, without CL (inhibition effects) and with CL. (g) Illustration of cooperative learning. A conceptual optoelectronic neuron is shown, which comprises an optical signaling unit for sensing and emitting optical signals. (h) The top panel is a schematic illustration of a self-organized map. The output neurons are WTA optoelectronic neurons. In such a network, the weighted inputs from the input layer provide a feedforward signal to the WTA neurons. Learning occurs through a cooperative scheme, in which the winning neuron uses a spatially constrained optical feedback signal. Only the synaptic weights of the winner and the neurons within the receptive field of the optical signal are updated. The bottom panel illustrates the WTA neurons and a decrease in the size of the receptive field as the problem is iteratively solved. (i) Top panel: A traveling sales person optimization problem is solved using this scheme. Here, the inputs to the self-organized map are the geographical coordinates of the cities in Switzerland. The goal is to compute the optimal route across the labeled cities, which is achieved by iteratively updating the synaptic connections of the WTA neurons. With learning, each WTA neuron gets attributed to a unique city, with its synaptic weights equaling the geographical coordinates. The bottom panel is the computed optimal route (distance).